PHYSICAL REVIEW B **79**, 054426 (2009)

Static and dynamic magnetic properties of $Ni_{80}Fe_{20}$ square antidot arrays

D. H. Y. Tse,* S. J. Steinmuller, T. Trypiniotis, D. Anderson, G. A. C. Jones, J. A. C. Bland, and C. H. W. Barnes
Department of Physics, Cavendish Laboratory, University of Cambridge, J. J. Thomson Avenue, Cambridge CB3 0HE, United Kingdom
(Received 26 November 2008; revised manuscript received 8 January 2009; published 20 February 2009)

We have investigated both static and dynamic magnetic properties of square antidot arrays in a ferromagnetic thin-film structure of Au (2 nm)/$Ni_{80}Fe_{20}$ (27.6 nm) on a SiO_2 500 nm/Si substrate using magneto-optic Kerr effect magnetometry, Brillouin light scattering (BLS), and micromagnetic simulations. The antidot patterns were 1 μm square holes arranged in two separate square lattices of dot separations $d=0.6$ μm and 1.0 μm. The introduction of antidots induced an in-plane fourfold magnetic anisotropy with hard axes on the two nearest-antidot-neighbor directions. The coercive field, H_c, was increased by the presence of antidots. Fixed-frequency modes were observed in spin-wave dispersion relations in remanent spin configurations. These modes correspond to spin-wave confinement by antidot edges, which were seen as a series of nodal lines parallel to the edges in simulated spin-wave mode spatial mappings. Domains in remanent states, some of which were responsible for the existence of dipole-exchange backward volume modes seen in BLS spectra, were also found to confine spin waves in simulations.

DOI: 10.1103/PhysRevB.79.054426 PACS number(s): 75.75.+a, 75.60.−d, 78.35.+c, 75.30.Ds

I. INTRODUCTION

Ferromagnetic thin films with arrays of antidots have generated considerable scientific interest in the last decade.[1–13] Patterning holes into ferromagnetic thin films is a simple yet effective way to engineer magnetic properties. Antidots alter demagnetizing fields in thin-film structures and at the same time they also pin domain walls. These two antidot characteristics are known to influence anisotropies,[1,2] switching characteristics,[3] coercivities,[4–7] and remanences[8,9] of ferromagnetic thin films. As well as being model systems for fundamental studies, antidot films also have the potential for storage applications as simulations have predicted that they could provide storage densities up to the order of ~ 0.1 Tb cm^{-2}.[14] Reading and writing speeds in magnetic storage devices, which are of the order of ~ 0.5 Gb s^{-1} currently,[15] are getting closer to the time scale of spin dynamics, as they are being continuously improved to meet ever increasing demands. They are ultimately limited by the frequency of spin precession.[16] Therefore, understanding of the dynamic magnetic properties of antidot films is important for the development of future devices.

Studies of spin dynamics in positive dot and wire structures have shown spin-wave confinement by lateral boundaries[17–19] and domain walls.[20] Previously, we have observed spin-wave mode splitting in antidot structures due to the spatial variation in the demagnetizing field.[11] However, confinements similar to those found in positive patterns were not observed, even though the lateral edges of antidot is expected to have the same spin-wave bounding effect. In this study, we look for the spin-wave confinement by the lateral boundaries of antidots. We first investigate different spin configurations found in antidot patterns by magneto-optic Kerr effect (MOKE) magnetometry and static micromagnetic simulation. Then we utilize the static results in combination with Brillouin light scattering (BLS) to study the effects of the spatial variations in spin alignment and lateral boundaries on spin dynamics, especially in remanent states which mimic the conditions in storage devices. The dynamic results are quantified by dynamic micromagnetic simulations to visualize the spatial distribution of spin-wave modes.

II. METHODS

The antidot arrays were patterned by a lift-off procedure. A layer of polymethyl methacrylate (PMMA) resist was spun onto a piece of thermally oxidized silicon wafer with the oxide 500 nm thick. The PMMA layer was patterned by electron-beam lithography and then developed to leave an array of square 1×1 μm^2 pillars. The patterned substrate was loaded into an ultrahigh vacuum (UHV) chamber for molecular-beam epitaxy (MBE). A $Ni_{80}Fe_{20}$ layer, approximately 30 nm thick, was deposited onto the patterned substrate using an electron-beam evaporator at a growth rate of ~ 0.3 nm min^{-1}. The base pressure and the growth pressure were 2.2×10^{-10} mbar and 1.2×10^{-9} mbar, respectively, and the whole process was conducted at room temperature (RT). Immediately after the $Ni_{80}Fe_{20}$ deposition, a 2 nm thick Au layer was deposited at similar conditions to prevent oxidation of the $Ni_{80}Fe_{20}$ layer. Finally, the PMMA pillars were lifted off in acetone, leaving antidot arrays.

Two square lattices of antidot arrays with separations $d=0.6$ μm and $d=1.0$ μm, as well as a continuous film for comparison, were prepared. The antidot dimensions were 1.0×1.0 μm^2. The overall area of each array was 672×672 μm^2. After the lift-off process, the patterns were checked by both optical microscopy and scanning electron microscopy (SEM) to ensure a successful lift off and correct dimensions. The SEM images of the two patterns can be found in Fig. 1. Analyzing a SEM image of an antidot tilted at 75°, the total thickness of the film was found to be 29.6 ± 0.2 nm. Assuming the Au layer was correctly grown 2 nm thick, the thickness parameter l of the $Ni_{80}Fe_{20}$ layer was set to 27.6 nm in later analysis.

Hysteresis loops of these arrays were obtained by MOKE magnetometry in the longitudinal geometry.[21] MOKE magnetometry uses changes in polarization and/or intensity when light is reflected from a magnetic material. In the longitudi-

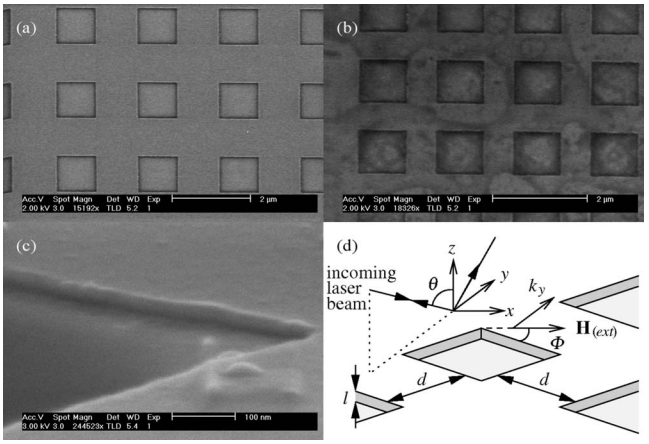

FIG. 1. SEM images and schematic of antidot samples. The square antidot area is 1×1 μm^2. (a) and (b) are antidots in square lattices with separations $d=1.0$ μm and $d=0.6$ μm, respectively. (c) shows a close up of an antidot taken with the sample tilted at 75°, and hence the side wall inside the antidot could be seen. The image was analyzed line by line, and the total thickness of the film was found to be 29.6 ± 0.2 nm. (d) is a schematic of the antidot pattern. It shows the geometry and parameters defined for MOKE and BLS measurements as well as for OOMMF simulations.

nal MOKE geometry, an external magnetic field $\mathbf{H}_{(ext)}$ is applied in the film plane and in the plane of the incident light, and it is sensitive to the in-plane component of the magnetization. The MOKE was characterized by polarimetry using a light source from a HeNe laser of wavelength 632.8 nm. The change in light polarization by MOKE in the reflected beam is converted to a change in the light intensity by an analyzer and the effect was measured as a function of $\mathbf{H}_{(ext)}$. Hysteresis loops for these samples were measured by varying $H_{(ext)}$ step by step from a positive value, which was high enough to saturate the sample, to the corresponding negative value and then back again. Hysteresis loops were obtained at $\Phi=0°$ and $\Phi=45°$, where Φ is the angle of $\mathbf{H}_{(ext)}$ with respect to the edge of antidots.

The spin-wave modes in these antidot structures were probed with BLS, which works by analyzing frequency shifts of photons involved in magnon scattering. Frequency shifts of the scattered light were resolved by a Sandercock 3+3 pass tandem Fabry-Pérot interferometer and then detected by a photomultiplier tube housed within a thermoelectric cooling holder. The scattered light was spatially filtered before entering the interferometer to suppress background noise, e.g., diffraction spots from the antidot array. Detailed descriptions of the operation of the interferometer as well as the data-acquisition system can be found in Ref. 22.

Measurements were carried out in the Voigt geometry where the applied field $\mathbf{H}_{(ext)}$ is in the plane of the sample and perpendicular to the plane of incidence of the beam. The coordinate system with respect to the scattering geometry is defined in Fig. 1(d). $\mathbf{H}_{(ext)}$ defines the **x** direction. **y** is perpendicular to **x** and in the planes of both the sample and the incidence of the laser; **z** is the plane normal. Only backscattered photons, i.e., those with paths changed roughly by 180°, were collected by the lens into the interferometer. Hence, the wave vector of the magnon being probed is in the **y** direction and its magnitude is given by $k_y=\frac{4\pi}{\lambda}\sin\theta$, where λ is the photon wavelength and θ is the photon incident angle. An Ar^+ ion single-mode laser of $\lambda=514.5$ nm and power 150 mW was used as the photon source. θ was varied from 12° to 60°, which converted to a range of $k_y=0.5\times10^5-2.1\times10^5$ cm^{-1}. All measurements were carried out at RT with $\Phi=0°$ or $\Phi=45°$.

Spin configurations in these antidots at different points along their hysteresis loops are determined using micromagnetics. Dipolar interactions, exchange interactions, magnetocrystalline anisotropies, and externally applied fields all contribute to the energy of a particular spin configuration. Equilibrium spin configurations are those at energy minima and transition paths between them are described by the Landau-Lifshitz-Gilbert (LLG) equation,[23,24] which is the equation of spin-motion,

$$\frac{\partial\mathbf{M}}{\partial t}=-\gamma\mathbf{M}\times\mathbf{H}_{(\mathrm{eff})}+\frac{\alpha}{M_s}\mathbf{M}\times\frac{\partial\mathbf{M}}{\partial t}, \tag{1}$$

where **M** is the magnetization, γ is the gyromagnetic ratio, α is the damping coefficient, M_s is the saturation magnetization, and $\mathbf{H}_{(\mathrm{eff})}$ is the effective magnetic field, including all the interactions mentioned above, acting on spins. Antidot patterns in 3×3 arrangements were divided into a regular two-dimensional grid of 10×10 nm^2 squares. The three-dimensional **M** positioned at the center in each cell is assumed to be uniform throughout the cell and discontinuous at cell boundaries. **M** in each cell as a function of time is found by integration of the LLG equation, which is done numerically using computational codes provided by the Object Oriented MicroMagnetic Framework (OOMMF).[25] As the boundary condition in OOMMF is aperiodic, simulation results from cells within a distance of 0.5 μm, i.e., 50 cells, from pattern boundaries were discarded as a workaround to any undesirable edge effects that might have occurred.

In a static simulation, $\mathbf{H}_{(ext)}$ as well as spins in antidot patterns were set initially aligned to one direction, which was either at $\Phi=0°$ or $\Phi=45°$ as is the case in MOKE and BLS measurements. $\mathbf{H}_{(ext)}$ was then reduced in steps of 1 Oe until all spins were saturated in the direction opposite to the initial alignment. At each step, an equilibrium spin configuration was assumed when the normalized torque value $|\mathbf{M}\times\mathbf{H}_{(\mathrm{eff})}|<10^{-5}$, which corresponds to an energy minimum.

As well as equilibrium spin configurations, OOMMF was also used to find spatial variations in spin-wave modes across these antidot patterns. At the starting point of a dynamic simulation, spin waves were excited in an equilibrium spin configuration by a small perturbation, which was in the form of a field pulse. The field pulse had a sinusoidal spatial profile and a Gaussian temporal profile, and it was defined by

$$h(k_y,t)=h_0\sin(k_y y)\exp\left[-\frac{4\ln(2)(t-2\sigma)^2}{\sigma^2}\right], \tag{2}$$

where h_0 is the pulse amplitude, y is the position in the grid along the direction of the wave vector, and σ is the temporal full width half maximum (FWHM) of the pulse. $h_0=10$ Oe and $\sigma=1$ ps were used in our simulations. The perturbation was chosen to simulate the condition in BLS where the wave

vector of the excited spin wave is the independent variable and is selected by k_y in Eq. (2). In a dynamic simulation, instead of recording the spin configuration when $|\mathbf{M} \times \mathbf{H}_{(\mathrm{eff})}| < 10^{-5}$, it was sampled with a regular period Δt_s in the simulation time. **M** averaged over the entire pattern was sampled every 5 ps. For individual cells in the two-dimensional grid, **M** was sampled every 25 ps, except for $H_{(\mathrm{ext})}=4$ kOe simulations in which $\Delta t_s=15$ ps. The power spectrum $\tilde{P}_z(x,y,f)=|\tilde{M}_z(x,y,f)|^2$ of the oscillation in the out-of-plane direction, **z**, in a particular cell was found by discrete Fourier transform,

$$\tilde{M}_z(x,y,f) \equiv \sum_{n=0}^{N-1} M_z(x,y,n\Delta t_s)\exp\left(\frac{2\pi i f n \Delta t_s}{N}\right), \qquad (3)$$

where N is the number of sampling points. The fast Fourier transform (FFT) algorithm was used to perform the discrete Fourier transform. Before applying the FFT, $M_z(x,y,t)$ was zero padded to at least double its sampling length to insulate the data from artifacts of undesired periodicity. Also they were filtered by the Hann window, $w_t=\frac{1}{2}[1-\cos(\frac{2\pi t}{N})]$, to reduce the leakage of frequency components into neighboring bins due to the finite length of the sample. The overall spectrum of a particular antidot pattern was found from the FFT of M_z averaged over the entire pattern. Spatial mappings of spin-wave modes were obtained from the FFT of M_z in all cells across the whole two-dimensional grid.

Material parameters required for the simulations described above were the exchange constant A, the anisotropy constant K, α, M_s, and γ. $A=1.3\times10^{-6}$ erg cm^{-1} is a typical value for $Ni_{80}Fe_{20}$. The isotropic nature of this material meant $K=0$ erg cm^{-3}. The choice of α is dependent on the time scale of simulations. $\alpha=0.5$ was used in static simulations; $\alpha=0.001$ was used in dynamic simulations. The last two parameters for $Ni_{80}Fe_{20}$, $M_s=622$ emu cm^{-3} and $\gamma=1.906\times10^7$ Hz Oe^{-1}, were obtained from fitting the Damon-Eshbach (DE) surface mode dispersion[26] to field-dependent BLS results from the continuous film grown at the same time as the antidot patterns.

III. RESULTS

Hysteresis loops of a continuous film and two antidot patterns are shown in Fig. 2 and their corresponding coercive fields, H_c, as well as remanence, $M_{x(\mathrm{rem})}/M_s$, are summarized in Table I. The hysteresis loops of the continuous film measured at $\Phi=0°$ and $\Phi=45°$ have the same square shape with low H_c. The presence of antidots in these permalloy films increases H_c. In general, H_c increases with decreasing d for both Φ angles. Figure 2 and Table I also show the results of hysteresis loop simulations using OOMMF. Simulated loops recreate the general trend of increasing H_c with decreasing d. Figure 3 shows simulated spin configurations in the two antidot patterns of separations $d=0.6$ μm and $d=1.0$ μm. These spin configurations, or domain patterns, are obtained along the upper part of hysteresis loops, i.e., $H_{(\mathrm{ext})}$ being changed from +500 Oe step by step to −500 Oe.

Figure 4 shows external field, $H_{(\mathrm{ext})}$, dependent spin-wave frequency measured by BLS at $k_y=1.73\times10^5$ cm^{-1}. In order

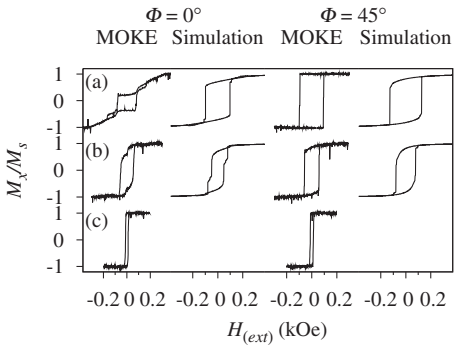

FIG. 2. Hysteresis loops of antidot patterns and a continuous film obtained by MOKE measurements and static OOMMF simulations. $\mathbf{H}_{(\mathrm{ext})}$ was applied at either $\Phi=0°$ or $\Phi=45°$ w.r.t. the edge of antidot. (a) and (b) are results from antidot patterns of separations $d=0.6$ μm and $d=1.0$ μm, respectively. (c) is the MOKE result for the continuous film.

to reproduce conditions and spin configurations in the upper arm of hysteresis loops, samples were initially saturated at $H_{(\mathrm{ext})}=+4.0$ kOe and then $H_{(\mathrm{ext})}$ was reduced step by step to the set value for measurements. Figure 4(a) shows the continuous film results at both $\Phi=0°$ and 45°. Spin-wave frequencies, f, at both Φ angles show almost no difference for the same set of experimental parameters. Assuming that both $\mathbf{H}_{(\mathrm{demag})}$ and K in the $Ni_{80}Fe_{20}$ film are negligible, these data were fitted to the DE surface mode dispersion [Eq. (4)] with M_s and γ as fitting parameters. This gives $M_s=622\pm2$ emu cm^{-3} and $\gamma=(1.906\pm0.004)\times10^7$ Hz Oe^{-1}, which is equivalent to a $Ni_{80}Fe_{20}$ g factor, $g=2.167\pm0.005$.

Figures 4(b) and 4(c) show $H_{(\mathrm{ext})}$-dependent BLS results from the antidot pattern of $d=0.6$ μm. f measured at $\Phi=0°$ [Fig. 4(b)] is close to the fitted curve from the continuous film. Its $H_{(\mathrm{ext})}$ dependence is very much similar to that in the continuous film. f measured at $\Phi=45°$ [Fig. 4(c)] is lower than the fitted values from the continuous film, and it deviates further away from the fitted curve as $H_{(\mathrm{ext})}$ is reduced.

$H_{(\mathrm{ext})}$-dependent BLS results from the $d=1.0$ μm antidot pattern are shown in Figs. 4(d) and 4(e). f measured at both $\Phi=0°$ and 45° is close to the fitted curve from the continuous film, apart from at $H_{(\mathrm{ext})}=0$ Oe, where f is lower than the fitted value. At $\Phi=45°$, f is also lower than the fitted values from the continuous film and deviates away from the fitted curve as $H_{(\mathrm{ext})}$ is reduced, similar to the $d=0.6$ μm case.

Figure 4 also includes OOMMF simulation results for all four antidot cases above. In some cases OOMMF underestimated f, however it reproduced trends in f as $H_{(\mathrm{ext})}$ is reduced.

Figure 5 shows dispersions of spin waves at $H_{(\mathrm{ext})}=0$ Oe in $d=0.6$ μm and 1.0 μm antidot patterns at $\Phi=0°$ and 45°. In general, the main peaks in the BLS spectra are found near frequencies predicted for a continuous film using Eq. (4). However, peaks at frequencies other than the continuous film frequency were also observed. There are two types of dispersions observed from these extra peaks in the spectra. First, a low-frequency mode ($f<5$ GHz) with slightly negative dispersion gradient at low k_y is seen in the

TABLE I. Coercive fields, H_c (Oe), and remanence, $M_{x(\mathrm{rem})}/M_s$, of antidot patterns and continuous film obtained from MOKE hysteresis loops and OOMMF simulations shown in Fig. 2. Errors in H_c (Oe) and $M_{x(\mathrm{rem})}/M_s$ are 1 Oe and 0.03, respectively.

	H_c (Oe)				$M_{x(\mathrm{rem})}/M_s$			
	$\Phi=0°$		$\Phi=45°$		$\Phi=0°$		$\Phi=45°$	
d (μm)	Expt.	Sim.	Expt.	Sim.	Expt.	Sim.	Expt.	Sim.
0.6	80	97	93	126	0.29	0.71	1.00	0.82
1.0	54	49	58	78	0.69	0.71	0.91	0.82
Film	12		12		0.98		0.99	

$d=0.6$ μm antidot pattern at both Φ angles and in the $d=1.0$ μm antidot pattern at $\Phi=0°$. Second, sets of fixed-frequency modes are seen clustering around the estimated continuous film frequency in both antidot patterns and both Φ angles. These fixed-frequency modes match those observed in OOMMF simulations. The frequencies and the range of k_y in which these modes are observed in simulations are also plotted in Fig. 5.

Figure 6 shows the micromagnetically simulated spatial mapping of fixed-frequency modes which are observed in both BLS and simulations. They are classified according to the number of nodes, n, found between the edges of two antidots.

IV. DISCUSSION

The continuous film showed small H_c and perfect squareness at both Φ angles. It has typical soft and isotropic magnetic characteristics as expected for a $Ni_{80}Fe_{20}$ film. Since the material itself does not possess an intrinsic magnetic anisotropy, any static or dynamic magnetic anisotropies found in antidot patterns must be attributed to the shape and the

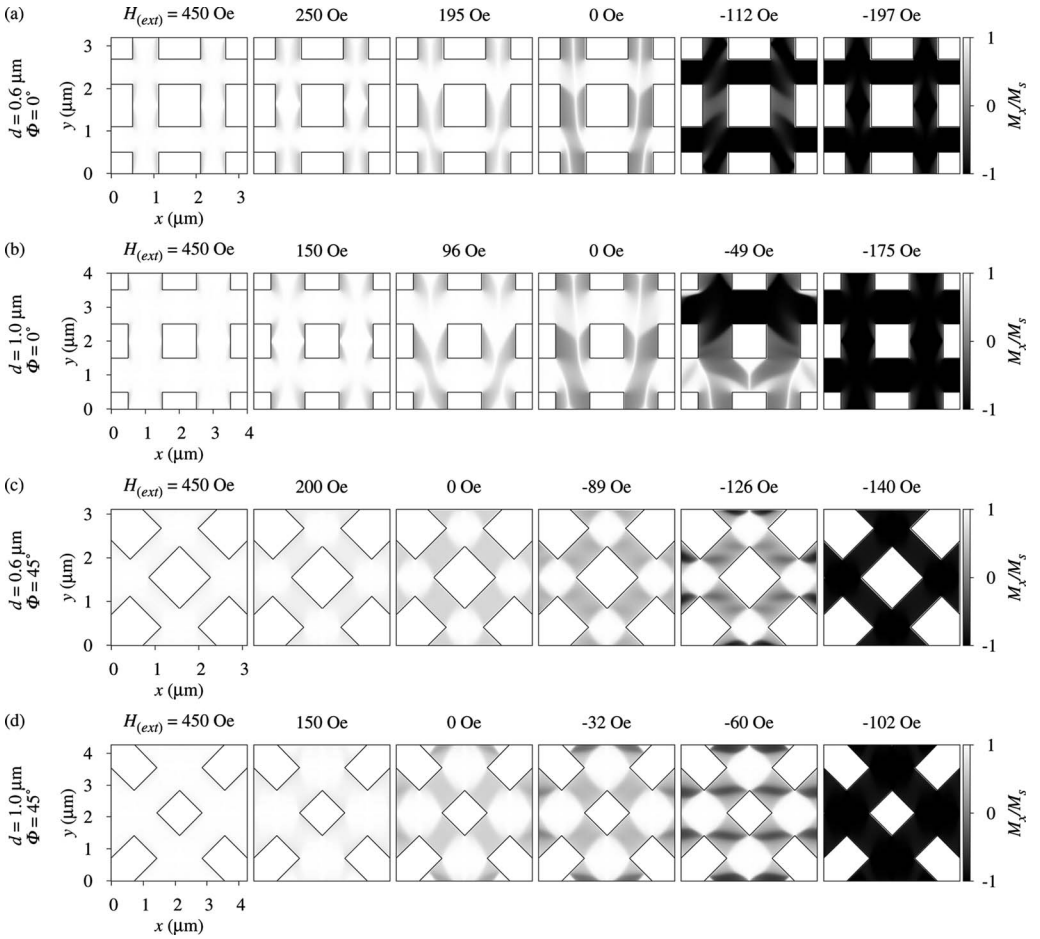

FIG. 3. OOMMF simulated spin configurations in antidot patterns at various points along the upper part of their hysteresis loops, i.e., $H_{(\mathrm{ext})}$ being changed from +500 Oe in steps of 1 Oe to −500 Oe.

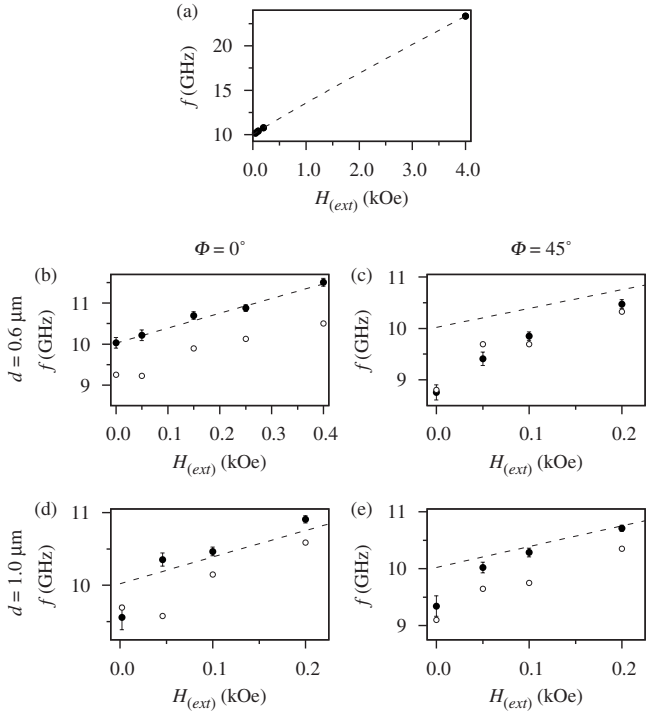

FIG. 4. External field, $H_{(\mathrm{ext})}$, dependent spin-wave frequency measured by BLS from antidot structures and a continuous film at $k_y = 1.73 \times 10^5$ cm^{-1}. (a) shows the whole range of continuous film data which were fitted to Eq. (4) with M_s and γ as parameters. ● are data from BLS measurements and (– – –) is the fitted curve. (b) and (c) are results from antidot patterns of $d = 0.6$ μm at $\Phi = 0°$ and 45°, respectively. (d) and (e) are results from antidot patterns of $d = 1.0$ μm at $\Phi = 0°$ and 45°, respectively. In (b)–(e), ● are data from BLS measurements and ○ are calculated frequencies from OOMMF simulations. Only the mode with frequency closest to that of the DE mode in the continuous film is shown here for clearer comparisons. (– – –) is the fitted curve for the continuous film.

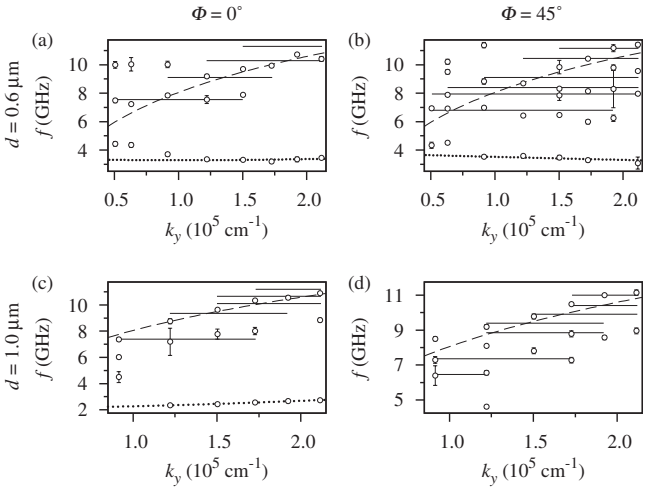

FIG. 5. Spin-wave dispersions in antidot structures at $H_{(\mathrm{ext})} = 0$ Oe. (a) and (b) are dispersion data from antidot patterns of $d = 0.6$ μm at $\Phi = 0°$ and 45°, respectively. (c) and (d) are dispersion data from antidot patterns of $d = 1.0$ μm at $\Phi = 0°$ and 45°, respectively. (– – –) is the dispersion curve calculated for a continuous film using Eq. (4). (—) are standing-wave frequencies as observed in micromagnetic simulations. These lines cover the range of k_y in which these fixed-frequency modes are found in simulations. (···) are fitted dispersion curves for dipole-exchange backward volume modes using Eq. (6).

arrangement of antidots. It has been shown that in arrays of circular antidots, in which the antidot shape contribution is isotropic, magnetic hard axes are found along the nearest-antidot-neighbor directions.[1,2] In a square lattice arrangement of edge aligned square antidots, a fourfold symmetry is anticipated and therefore the greatest difference in magnetic properties is expected at $\Phi = 0°$ and 45°. Increases in H_c, $M_{x(\mathrm{rem})}/M_s$, and squareness in hysteresis loops of both patterns are seen at $\Phi = 45°$ (Fig. 2 and Table I). This evidence suggests that the hard axis is at $\Phi = 0°$, which agrees with the nearest-antidot-neighbor rule.

As well as reduced squareness, multiple switchings are seen in hysteresis loops at $\Phi = 0°$. To gain an insight into different shapes of hysteresis loops at the two Φ angles, spin configurations from static OOMMF simulations (Fig. 3) need to be considered. At $\Phi = 0°$, the whole process can be divided into three interlinked processes in three different regions of the antidot pattern. Longitudinal regions behave very much like hard axis elements because of the increased $H_{(\mathrm{demag})}$ in the presence of antidot edges perpendicular to $\mathbf{H}_{(\mathrm{ext})}$. Domains with spins perpendicular to $\mathbf{H}_{(\mathrm{ext})}$ nucleate from antidot edges and then grow in size to dominate the whole region at remanence. In the hysteresis loop, this reversible process[3] is seen as the gradual decrease in M_x/M_s from saturation when $H_{(\mathrm{ext})}$ is reduced. Just before $H_{(\mathrm{ext})}$ is reduced to 0 Oe, spins in crossover regions switch by 90° from the $\mathbf{H}_{(\mathrm{ext})}$ direction, allowing domains in neighboring longitudinal regions to join together. This process appears as the small jump before $H_{(\mathrm{ext})} = 0$ Oe in the hysteresis loop. Latitudinal regions switch with an easy-axis-type spin reversal in which spins are initially aligned to $\mathbf{H}_{(\mathrm{ext})}$ until H_c is reached where all spins flip by 180°. This is an irreversible process[3] and is observed as the major jump in the hysteresis loop. Hence, small hints of easy axis type switching is seen in the hysteresis loop, even though $\Phi = 0°$ is the overall hard axis.

At $\Phi = 45°$, only two different switching processes occur. Spins in crossover regions switch in the same manner as in latitudinal regions at $\Phi = 0°$, which is an easy-axis-type spin reversal. In diagonal regions, as $H_{(\mathrm{ext})}$ is being reduced to 0 Oe, spins rotate away from the $\mathbf{H}_{(\mathrm{ext})}$ direction to align with the 45° edges, resulting in a minimal $H_{(\mathrm{demag})}$ in these diagonal regions. As $H_{(\mathrm{ext})}$ approaches $-H_c$, spins in diagonal regions rotate toward the $\mathbf{H}_{(\mathrm{ext})}$ direction and small domains in which spins parallel to $\mathbf{H}_{(\mathrm{ext})}$ start to nucleate. Finally at $-H_c$, all spins flip to the $\mathbf{H}_{(\mathrm{ext})}$ direction. This also triggers the spin reversal in crossover regions, and hence only a single switching is seen in the hysteresis loops. The combination of spin rotation and flipping at H_c in diagonal regions suggests that the switching in these regions is an intermediate between the hard axis and easy axis types, leading to a high $M_{x(\mathrm{rem})}/M_s$ and an overall easy axis at $\Phi = 45°$. Switching processes in individual regions at both Φ angles depend on $\mathbf{H}_{(\mathrm{demag})}$, which itself is dependent on the alignment of antidot edges with respect to $\mathbf{H}_{(\mathrm{ext})}$. Therefore, the anisotropy arises from the shape of antidots and the arrangement of antidot arrays.

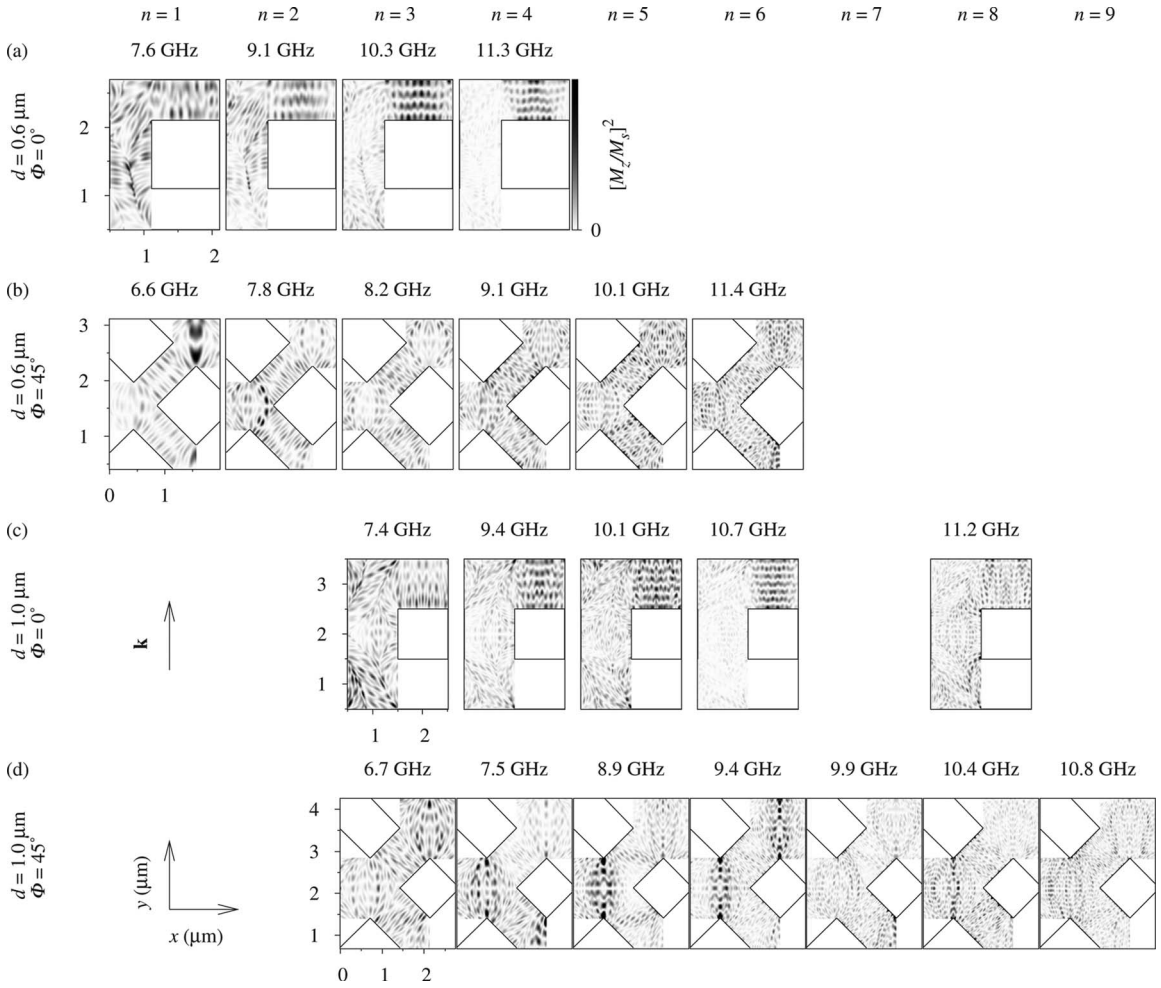

FIG. 6. Spatial mappings of spin-wave modes in antidot structures at $H_{(ext)}=0$ Oe obtained from OOMMF simulations. n is the number of nodes found across the edges of the pattern.

Another effect of the presence of antidots is the increase in H_c in both Φ-angle hysteresis loops. The presence of antidots introduced huge areas of ferromagnet-to-air boundaries into the magnetic film. These boundaries modify the demagnetizing field $H_{(demag)}$ distribution and profile in the film. At the same time, these boundaries act as domain-wall pinning sites. Both of these properties of antidots have been linked to the extra H_c in antidot patterns compared with the continuous film and to the increase in H_c with increasing antidot density.[4–7] Both measured and simulated H_c shown in Table I agree with the phenomenological approximation $H_c \propto 1/d$ stated in Ref. 6. This relationship follows the idea that the closer the antidots are, the stronger the effects of $H_{(demag)}$ and domain-wall pinning are, and therefore the higher the $H_{(ext)}$ required to overcome them.

OOMMF simulations (Fig. 3) show that antidot patterns of different d go through comparable stages of spin configuration. However these comparable stages occur at higher magnitude of $\mathbf{H}_{(ext)}$ for smaller d, which agrees with the observed modifications in the shape of MOKE hysteresis loops (Fig. 2). As d is varied, effects of $H_{(demag)}$ and domain-wall pinning play different roles in modifying switching processes, which ultimately lead to changes in the shape of hysteresis loops. At $\Phi=0°$, the overall $H_{(demag)}$ in longitudinal regions increases with decreasing d when all spins are aligned to $\mathbf{H}_{(ext)}$. As $H_{(ext)}$ is reduced, spins in longitudinal regions rearrange to the configuration which minimizes the overall energy from $H_{(demag)}$. This process occurs at higher $H_{(ext)}$ as d is reduced. Therefore, more of a hard axis characteristic is seen in the $\Phi=0°$ hysteresis loop of the $d=0.6$ μm antidot pattern. For the same reason, spins in diagonal regions at $\Phi=45°$ get more difficult to rotate as d decreases. Hence, the $\Phi=45°$ hysteresis loop becomes more like an easy axis loop as d changes from 1.0 μm to 0.6 μm.

Domain-wall pinning stabilizes certain local spin configurations. The increased domain-wall pinning in the $d=0.6$ μm antidot pattern stabilizes domains in longitudinal regions, which caused M_x/M_s in the $\Phi=0°$ hysteresis loop to stay constant from $H_{(ext)}=80$ Oe to $-H_c$. Also, the increased domain stability in longitudinal regions prevents spins in these regions from reversing completely at H_c, which is seen in the $d=0.6$ μm antidot pattern.

Static OOMMF simulations provide insights into the various spin configurations along the cycle of hysteresis loops. Nonetheless, they only reproduced a few of the features seen in MOKE hysteresis loops. Although H_c obtained from simulations agreed with the phenomenological approximation $H_c \propto 1/d$, it tends to be overestimated. The simulations also

failed to predict small jumps in the $\Phi=0°$ hysteresis loop of the $d=0.6$ μm antidot pattern. These jumps are predicted by the simulation for the $d=1.0$ μm antidot pattern, but the $H_{(\mathrm{ext})}$ value at which these jumps occur and the range of M_x/M_s changed are not accurately reproduced. Remanent spin configurations should depend on Φ,[8] as well as on d and the dimensions of the antidot.[9] These properties are implicated from MOKE hysteresis loops (Fig. 2). Simulated spin configurations at remanence vary with Φ, but they do not vary significantly with d. All these mismatches indicate that energy contours around possible spin configurations are different in experimental and simulated conditions. One of the missing conditions in simulations is thermal fluctuations. Hence spin configurations are effectively being simulated at 0 K. Switching between two spin configurations at H_c or at other small jumps in the hysteresis loop could be assisted by thermal fluctuations to overcome the energy barrier between the two states. Also simulating a small portion of the whole antidot pattern introduces an edge effect which modifies $\mathbf{H}_{(\mathrm{demag})}$ and creates nucleating sites near the edges of the simulation pattern, leading to erroneous results.

The continuous film also does not show any anisotropy in spin-wave frequency, f, as expected for $Ni_{80}Fe_{20}$. Its f dependence on $H_{(\mathrm{ext})}$ fitted well[27] to the DE surface mode dispersion,[26]

$$f=\frac{\gamma}{2\pi}\sqrt{H_{(\mathrm{ext})}(H_{(\mathrm{ext})}+4\pi M_s)+\frac{(4\pi M_s)^2}{2+2\coth(k_y l)}}, \quad (4)$$

with M_s and γ as fitting parameters. Fitting results match with typical values for $Ni_{80}Fe_{20}$, with M_s agreeing within errors to the tabulated value in Ref. 28, and γ being higher than the reported value in Ref. 29 by 3%.

Equation (4) is derived for a thick slab of infinite lateral extent in which the magnetization $\mathbf{M}$ is in-plane, uniform, and perpendicular to the in-plane spin-wave wave vector $\mathbf{k}_\parallel$. The presence of antidots and formation of domains at low $H_{(\mathrm{ext})}$, as seen in previous sections, alter the spin-wave characteristics from the description of Eq. (4) in several ways. First, domain walls act as boundaries confining spin-wave modes as well as separating regions with different dispersion characteristics due to the variation in the angle between $\mathbf{k}_\parallel$ and $\mathbf{M}$ from one domain to another.[10,20] Second, edges of antidots provide ferromagnet-to-air boundaries for lateral confinement of spin waves as seen in Refs. 13 and 17–19. Furthermore, these boundaries also modify the distribution and profile of $H_{(\mathrm{demag})}$ in the film which results in dipolar localization of spin waves.[11,12] Inhomogeneities in $H_{(\mathrm{demag})}$ near these boundaries can further confine an edge mode.[13,19,30,31]

Dynamic OOMMF simulations using equilibrium spin configurations allow all these conditions to be taken into account. Although simulations underestimated f in some cases, trends in the $H_{(\mathrm{ext})}$ dependence of f are well reproduced by simulations of the two antidot patterns at both Φ angles. At $\Phi=45°$, spins rotate away from the $\mathbf{H}_{(\mathrm{ext})}$ direction in diagonal regions when $H_{(\mathrm{ext})}$ approaches 0 Oe. As the angle between $\mathbf{M}$ and k_y becomes smaller, the observed spin waves have a stronger backward volume mode character and f decreases.[26] Therefore, f in both antidot patterns at $\Phi=45°$ deviates away from the curve predicted for the surface mode in a continuous film by Eq. (4) as $H_{(\mathrm{ext})}$ is reduced [Figs. 4(c) and 4(e)]. At $\Phi=0°$, the $H_{(\mathrm{ext})}$ dependence of f follows the curve fitted for the continuous film, except at $H_{(\mathrm{ext})}=0$ Oe for the $d=1.0$ μm antidot pattern. The exception can be linked to the presence of domains in the remanent spin configuration as well as to those ferromagnet-to-air boundaries provided by antidot edges. Further insights can be gained from spin-wave dispersion relations (Fig. 5) and their simulated spatial mappings (Fig. 6) in remanent spin configurations.

At $\Phi=0°$, antidot edges in latitudinal regions are perpendicular to the in-plane direction of scattering photons. Simulated spin-wave mode spatial mappings suggest that spin waves excited by incident photons are strongly confined by these two boundaries, resulting in fixed-frequency modes in the dispersion relations. The wave vectors $k_{y,n}$ of these modes are determined by the number of nodes n that can be fitted in a cavity of length d and the boundary condition of spin precession. Observed values of f and n of these fixed-frequency modes suggest that spins are neither fully pinned nor totally free at these boundaries. The wave vector of these modes can be described by

$$k_{y,n}=\frac{2\pi}{d}\left[\frac{1}{2}(n-1)+\psi\right], \quad (5)$$

where $0<\psi\leq 1$ and the proportion of the spin-wave amplitude at a boundary is given by $m_0=\sin(\psi\pi)$. By substituting Eq. (5) into Eq. (4) and comparing the results with values of f from fixed-frequency mode, m_0 is estimated to be 0.61 ± 0.04 at $\Phi=0°$. For a particular value of m_0 in the range $0<m_0<1$, there are two positions within a half wavelength which can fit to the boundary condition. Therefore, degeneracy of modes of different n can occur as it can be seen in the mode spatial mappings of the $d=1.0$ μm antidot pattern.

In simulated spin-wave mode spatial mappings, fixed-frequency modes are observed in latitudinal regions only, i.e., they are contained within individual domains. Domain walls provide a pair of spin-wave boundaries that roughly run parallel to the $\mathbf{y}$ direction. Standing spin waves are also seen in mode spatial mappings forming across these domain walls. The weak nodal lines resulting from domain-wall confinements suggest that these confinements are not fixed in position unlike in the case with antidot edges. This is because the domain walls themselves are mobile up to a certain point even in an equilibrium spin configuration, thus allowing standing-wave patterns to move. Furthermore, domain-wall motion is the likely origin of k_x in spin-wave modes excited from a perturbation that only has a y component.

At $\Phi=45°$ antidot edges are the spin-wave confinement boundaries for diagonal regions. As discussed above, only two positions within a half wavelength can suit the boundary condition. It means that nodal lines must line up with antidot edges being at 45° to the xy axes, which is seen in diagonal regions in simulated mode spatial mappings. Using Eqs. (4) and (5) with d replaced with $d\sqrt{2}$, $m_0=0.71\pm0.06$ is esti-

mated at $\Phi=45°$. Crossover regions are bounded by domain walls at 45° to the xy axes at all sides (Fig. 3). However nodal lines in crossover regions are rotated by 45° from those in diagonal regions, i.e., they are aligned with the xy axes. This infers that spin-wave amplitudes at domain-wall boundaries are not fixed at a particular value; instead they are coupled to spin waves on the other sides of the domain wall. This type of weak confinement allows spin waves in crossover regions to follow the profile of the perturbation [Eq. (2)], which has nodal lines parallel to the x axis.

The wave vector $k_{y,n}$ of confined spin waves has discrete values as described by Eq. (5). Hence $k_{y,n}$ does not necessarily conserve with the in-plane component of the scattering photon wave vector, k_y, in BLS. The scattering intensity, $I(k_y)$, as a function of k_y of the nth confined spin-wave mode with magnetization precession profile, $\mathbf{m}_n$, is proportional to the spatial power spectrum of $\mathbf{m}_n$,[17,32,33] i.e., $I(k_y) \propto |\tilde{\mathbf{m}}_n(k_y)|^2$. Since $\mathbf{m}_n$ has a sinusoidal profile with its extent limited by a top hat function, $I(k_y)$ has the form of a sinc^2 function with the peak at $k_{y,n}$, which means that fixed-frequency modes have the highest scattering intensity when k_y matches with $k_{y,n}$. Therefore, fixed-frequency modes are seen clustering around the continuous film curve in dispersion relations (Fig. 5). Also, the relationship $I(k_y) \propto |\tilde{\mathbf{m}}_n(k_y)|^2$ is reproduced in dynamic simulations because of the well-defined k_y sinusoidal spatial profile of the perturbation Eq. (2). The range of k_y was set to 0.5×10^5–2.1×10^5 cm^{-1} in both BLS and OOMMF simulations. Therefore, the increased confinement cavity length in the $d=1.0$ μm pattern results in confined modes with higher values of n being observed.

In dispersion relations in Fig. 5, a mode with frequencies lower than those of the DE mode is seen in the $d=0.6$ μm antidot pattern at both Φ angles and in the $d=1.0$ μm antidot pattern at $\Phi=0°$. This mode has a slightly negative dispersion gradient at low k_y. Both of these are characteristic of the dipole-exchange backward volume (DEBV) mode, which is observed in regions where $\mathbf{M}\|\mathbf{k}_\|$. The DEBV mode is not observed clearly in dynamic simulations due to the two-dimensional grid limitation. For nonzero surface spin pinning and for other higher order DEBV modes, there are amplitude and phase variations in the spin precession across the thickness of the film which would require a three-dimensional grid to model properly. However, spin configurations from static simulations indicate that the DEBV mode is expected to be found in longitudinal regions of antidot patterns at $\Phi=0°$ and in diagonal regions at $\Phi=45°$. In the $d=1.0$ μm antidot pattern at $\Phi=45°$, areas of domains in which $\mathbf{M}\|\mathbf{k}_\|$ are relatively small, and hence the DEBV mode intensity in BLS could have been too low to be observed. The dispersion of the DEBV mode given by[34]

$$f=\frac{\gamma}{2\pi}\sqrt{\left(H_{(\mathrm{ext})}+\frac{2A}{M_s}k_y^2\right)}\times\sqrt{\left(H_{(\mathrm{ext})}+\frac{2A}{M_s}k_y^2+\frac{4\pi M_s}{k_y l}(1-e^{-k_y l})\right)}, \quad (6)$$

was fitted to BLS data with the exchange constant A and the magnitude of demagnetizing field $H_{(\mathrm{demag})}$ in $H_{(\mathrm{ext})}$ as the fitting parameters. Estimated values for the two parameters are $A=(4\pm2)\times10^{-7}$ erg cm^{-1}, which is similar to values from Refs. 35 and 36, and $H_{(\mathrm{demag})}=140\pm40$ Oe, which is comparable to the spatially averaged value of $H_{(\mathrm{demag})}=100$ Oe calculated from spin configurations simulated in OOMMF in regions where the DEBV mode is expected to be found.

V. CONCLUSIONS

Static and dynamic magnetic properties of antidot patterns were studied with MOKE magnetometry, BLS, and OOMMF micromagnetic simulations. MOKE measurements have shown that the introduction of antidots induced an in-plane fourfold magnetic anisotropy with hard axes on the two nearest-antidot-neighbor directions. The anisotropy, which originated from the dependence of the angular demagnetizing field, $\mathbf{H}_{(\mathrm{demag})}$, on antidot shape and array arrangement, modified the switching processes in between spin configurations along a hysteresis loop. The coercive field H_c was increased by the presence of antidots. Simulations demonstrated that spin configurations along hysteresis loops stay unchanged between the two d values. However, the magnitude of external fields, $H_{(\mathrm{ext})}$, at which transitions between these spin configurations occur increased with decreasing d. This is attributed to the increased domain-wall pinning and a general increase in the magnitude of the demagnetizing field, $H_{(\mathrm{demag})}$, throughout the antidot pattern. BLS measurements have shown that properties of spin waves were altered by new spin configurations at low $H_{(\mathrm{ext})}$ in the presence of antidots. Fixed-frequency modes were observed in dispersion relations of spin waves in spin configurations at remanence. These modes correspond to standing spin waves confined by antidot edges. They were also seen in simulated spatial mappings with clear nodal lines parallel to antidot edges. Spin-wave amplitudes at these confinement boundaries were estimated to be 0.61 at $\Phi=0°$ and 0.71 at $\Phi=45°$ of the full amplitude. Confinement of spin waves by domain walls is also seen in simulations, which showed different confinement characteristics from those of antidot edges. The domain-wall spin-wave boundary has a small amount of mobility and the spin-wave amplitudes on both sides of a domain-wall boundary are coupled. Scattering intensities of these fixed-frequency modes in both BLS and simulations were proportional to the spatial power spectrum of the magnetization precession profile of these modes. DEBV modes, which have lower frequencies than the DE mode and have negative dispersion gradient at low wave-vector magnitude, k_y, were also observed in dispersion relations. They are expected to be observed in regions of antidot patterns where the magnetization is parallel to the in-plane wave vector.

ACKNOWLEDGMENT

This work has been supported by the EPSRC (UK).

*dhyt3@cantab.net

[1] C. T. Yu, H. Jiang, L. Shen, P. J. Flanders, and G. J. Mankey, J. Appl. Phys. **87**, 6322 (2000).
[2] P. Vavassori, G. Gubbiotti, G. Zangari, C. T. Yu, H. Yin, H. Jiang, and G. J. Mankey, J. Appl. Phys. **91**, 7992 (2002).
[3] L. J. Heyderman *et al.*, Phys. Rev. B **73**, 214429 (2006).
[4] A. O. Adeyeye, J. A. C. Bland, and C. Daboo, Appl. Phys. Lett. **70**, 3164 (1997).
[5] W. Y. Lee, H. T. Leung, W. Zhang, Y. B. Xu, A. Hirohata, C. C. Yao, B. C. Choi, D. G. Hasko, and J. A. C. Bland, IEEE Trans. Magn. **35**, 3475 (1999).
[6] I. Ruiz-Feal *et al.*, J. Magn. Magn. Mater. **242-245**, 597 (2002).
[7] C. C. Wang, A. O. Adeyeye, and Y. H. Wu, J. Appl. Phys. **94**, 6644 (2003).
[8] M. J. Van Bael, S. Raedts, K. Temst, J. Swerts, V. V. Moshchalkov, and Y. Bruynseraede, J. Appl. Phys. **92**, 4531 (2002).
[9] A. Y. Toporov, R. M. Langford, and A. K. Petford-Long, Appl. Phys. Lett. **77**, 3063 (2000).
[10] O. N. Martyanov, V. F. Yudanov, R. N. Lee, S. A. Nepijko, H. J. Elmers, R. Hertel, C. M. Schneider, and G. Schonhense, Phys. Rev. B **75**, 174429 (2007).
[11] S. McPhail, C. M. Gurtler, J. M. Shilton, N. J. Curson, and J. A. C. Bland, Phys. Rev. B **72**, 094414 (2005).
[12] M. H. Yu, L. Malkinski, L. Spinu, W. L. Zhou, and S. Whittenburg, J. Appl. Phys. **101**, 09F501 (2007).
[13] C. T. Yu, M. J. Pechan, W. A. Burgei, and G. J. Mankey, J. Appl. Phys. **95**, 6648 (2004).
[14] L. Torres, L. Lopez-Diaz, O. Alejos, and J. Iniguez, Physica B **275**, 59 (2000).
[15] D. Weller and A. Moser, IEEE Trans. Magn. **35**, 4423 (1999).
[16] T. Gerrits, H. A. M. van den Berg, J. Hohlfeld, L. Bar, and T. Rasing, Nature (London) **418**, 509 (2002).
[17] C. Mathieu *et al.*, Phys. Rev. Lett. **81**, 3968 (1998).
[18] J. Jorzick, S. O. Demokritov, B. Hillebrands, B. Bartenlian, C. Chappert, D. Decanini, F. Rousseaux, and E. Cambril, Appl. Phys. Lett. **75**, 3859 (1999).
[19] J. Jorzick, S. O. Demokritov, B. Hillebrands, M. Bailleul, C. Fermon, K. Y. Guslienko, A. N. Slavin, D. V. Berkov, and N. L. Gorn, Phys. Rev. Lett. **88**, 047204 (2002).
[20] K. Perzlmaier, M. Buess, C. H. Back, V. E. Demidov, B. Hillebrands, and S. O. Demokritov, Phys. Rev. Lett. **94**, 057202 (2005).
[21] Z. Q. Qiu and S. D. Bader, Rev. Sci. Instrum. **71**, 1243 (2000).
[22] B. Hillebrands, Rev. Sci. Instrum. **70**, 1589 (1999).
[23] L. D. Landau and E. Lifshitz, Phys. Z. Sowjetunion **8**, 153 (1935).
[24] T. L. Gilbert, Phys. Rev. **100**, 1243 (1955) [Abstract only; full report, Armor Research Foundation Project No. A059, Supplementary Report, May 1, 1956] (unpublished).
[25] M. J. Donahue and D. G. Porter, OOMMF v1.2a3 Object Oriented MicroMagnetic Framework, software (NIST, 2004), available at http://math.nist.gov/oommf
[26] R. W. Damon and J. R. Eshbach, J. Phys. Chem. Solids **19**, 308 (1961).
[27] Coefficient of multiple determination, R^2, being close to 1.
[28] G. W. C. Kaye and T. H. Laby, *Tables of Physical and Chemical Constants and Some Mathematical Functions*, 15th ed. (Longman, London, 1986).
[29] S. J. Barnett, Phys. Rev. **90**, 315 (1953).
[30] J. P. Park, P. Eames, D. M. Engebretson, J. Berezovsky, and P. A. Crowell, Phys. Rev. Lett. **89**, 277201 (2002).
[31] K. Y. Guslienko, R. W. Chantrell, and A. N. Slavin, Phys. Rev. B **68**, 024422 (2003).
[32] M. G. Cottam and D. J. Lockwood, *Light Scattering in Magnetic Solids* (Wiley, New York, 1986).
[33] J. Jorzick, S. O. Demokritov, C. Mathieu, B. Hillebrands, B. Bartenlian, C. Chappert, F. Rousseaux, and A. N. Slavin, Phys. Rev. B **60**, 15194 (1999).
[34] B. A. Kalinikos and A. N. Slavin, J. Phys. C **19**, 7013 (1986).
[35] C. H. Wilts and S. K. C. Lai, IEEE Trans. Magn. **8**, 280 (1972).
[36] N. Smith, D. Markham, and D. LaTourette, J. Appl. Phys. **65**, 4362 (1989).